Optics & Laser Technology 177 (2024) 111066

Contents lists available at ScienceDirect

Optics and Laser Technology

journal homepage: www.elsevier.com/locate/optlastec

Full length article

Design and implementation of dynamic beam shaping in high power laser processing by means of a Deformable Mirror

Scholte J.L. Bremer [a,*], Ronald G.K.M. Aarts [b], Gert-willem R.B.E. Römer [a]

[a] Chair of Laser Processing, Department of Mechanics of Solids, Surfaces & Systems, Faculty of Engineering Technology, University of Twente, Drienerlolaan 5, 7522NB, Enschede, The Netherlands

[b] Chair of Applied Mechanics and Data Analysis, Department of Mechanics of Solids, Surfaces & Systems, Faculty of Engineering Technology, University of Twente, Drienerlolaan 5, 7522NB, Enschede, The Netherlands

ARTICLE INFO

Keywords:
Beam shaping
Deformable mirror
High power
Laser material processing

ABSTRACT

Optimising the laser intensity distribution in high power laser processes, such as laser welding, laser cladding or laser hardening, can be used to tailor the local thermal fields and thermal cycles which, in turn, determine the final process results. Deformable Mirrors allow to dynamically shape the beam profile and previous studies showed their potential. However, only limited flexibility in achievable beam shapes is shown at higher power levels. In addition the relation between desired laser intensity profiles and required mirror surface profiles is nontrivial. In this work the design and implementation of a dynamic beam shaping system, capable of handling high laser powers (up to 1 kW), is presented and evaluated. To that end, several distinctly different laser intensity profiles are defined, corresponding mirror surfaces are determined and realised with the beam shaping system. Measurements of the laser intensity profiles were compared with laser intensity profiles simulated using a previously presented mathematical framework and showed a good agreement. From the measurements it was concluded that the setup is suitable for high laser powers (up to 1 kW) and is characterised by large depth of focus ($<$ 14% change in dimensions at a distance of 100 mm from the focal plane).

1. Introduction

In high power laser material processes, such as laser welding, laser cladding and laser hardening, a laser source is used to locally heat the substrate [1]. The final (material) properties of the product after laser processing are affected by the laser induced thermal cycles [2–4]. Traditionally these thermal cycles are optimised by adapting laser power [5,6], beam velocity [7,8] and (if applicable) material feed rate [9,10]. However, research shows that the distribution of the laser power – i.e. the power density distribution (PDD) or laser beam shape – strongly affects the local laser-induced thermal fields and therefore thermal cycles and the local thermal gradients [11,12].

Commonly axisymmetric uniform or Gaussian PDDs are employed in high power laser material processing [12,13]. Some studies adapted the PDD to improve the process or the processing results. One approach of beam shaping is using optical transport fibres with specific cross-sectional shapes of the fibre cores [11,14]. Also the use of diffractive optical elements [15,16] as a means of beam shaping is reported in literature. However, these approaches are *static* beam shaping methods. That is, these approaches do not allow to change the PDD during processing. Enabling this adaptation of the PDD during processing, i.e. dynamic beam shaping, allows to control or tailor thermal cycles in-situ.

To dynamically shape the laser beam, commonly beam oscillation is used. With a Galvanometer Scanner, a predefined pattern is scanned iteratively by the focal spot of the laser beam, such that an equivalent PDD is written. With this beam shaping device mainly Lissajous figure shaped beams are created [17,18], although also more arbitrary shapes can be generated [19]. Due to the scanning nature of this beam shaping approach, undesirable cooling of the material will appear between the consecutive passes of the laser beam. This undesired cooling can be reduced by increasing the scan frequencies of the Galvanometer mirrors. Another dynamic beam shaping approach which is also based on steering the laser beam over a predefined pattern is Coherent Beam Combining [20]. This technology allows to steer the beam at frequencies of 10 s of MHz [21]. However, this beam shaping technology is integrated with the laser source and there cannot be used for retrofitting already available laser sources.

A non-scanned dynamic beam shaping approach is the use of Multi Plane Light Conversion [22], however this approach allows only a few degrees of freedom. Also a Deformable Mirror (DM) can be used to

---

[*] Corresponding author.
E-mail address: s.j.l.bremer@utwente.nl (S.J.L. Bremer).

https://doi.org/10.1016/j.optlastec.2024.111066
Received 1 February 2024; Received in revised form 28 March 2024; Accepted 22 April 2024

dynamically shape the PDD [23]. Here the shape of the DM surface, controlled by a number of actuators, adapts the wavefront of the laser beam resulting in an adapted PDD in the focal spot of the laser beam [24]. Unfortunately the flexibility to create beam shapes for high laser power levels is yet limited to elliptic laser intensity profiles [23]. However, the potential for creating more complex PDDs has been shown for low powers [25]. To create more complex beam shapes, corresponding mirror surface profiles must be defined. For specific PDDs and Gaussian initial beam these mirror shapes are known [25]. For arbitrary PDDs, non-trivial algorithms to design freeform optical surfaces for general lightning applications [26] could be adapted, however these do not provide direct insight into how to shape the DM for a desired PDD. The inverse relation, i.e. computing the obtained PDD using a given mirror surface, is known [27].

To address the above issues, the objective of this work is to develop a high power beam shaping system. This beam shaping system will be a non-scanned approach with a high degree of freedom in shape of the generated PDDs. Furthermore it should be possible to integrate the beam shaping system in an existing focusing optic. Therefore this work proposes, in Section 2, a high power dynamic laser beam shaping system, based on a DM. In order to create several distinctly different beam shapes, corresponding mirror surfaces should be derived, which is addressed in Section 3. Next, in Section 4, our approach of beam shaping using the DM will be experimentally demonstrated at low and high laser power levels.

2. Experimental setup & layout of the beam shaping system

Section 2.1 presents and discusses the optical design layout of the beam shaping system using a DM. Section 2.2 details the used analysis equipment used to measure the created laser intensity profiles.

2.1. Optical layout & implementation

The focusing optics, including the beam shaping system, will be designed to be employed in combination with a multimode transport fibre. Conventionally, the focusing optic consists out of a collimator and focusing lens, as schematically shown in Fig. 1(a). In this case the PDD in the focal spot is an image of the cross-sectional area of the fibre core. The diameter of the focal spot d_f is determined by

$$d_\mathrm{f} = \frac{f_\mathrm{f}}{f_\mathrm{c}} d_0. \tag{1}$$

Here f_f denotes the focal length of the focusing lens, f_c denotes the focal length of the collimator, and d_0 is the fibre core diameter. In the beam path section between these lenses the beam diameter is constant, therefore it is convenient to integrate the DM within this section, which is schematically shown in Fig. 1(b). Here the diameter of the DM should match the collimated beam diameter d_c, defined as

$$d_\mathrm{c} = f_\mathrm{c}\theta_0, \tag{2}$$

where θ_0 is the far-field divergence angle at the fibre exit.

Besides the DM, also a Galilean beam reducer, consisting of a concave and a convex mirror, is added to the beam path. This beam reducer is required to magnify the dimensions of the PDD in the focal plane without increasing the focal length of the focusing lens. This combination of Galilean beam reducer and focusing lens results in a focusing lens with an equivalent focal length f_eq of

$$f_\mathrm{eq} = -\frac{f_1}{f_2} f_\mathrm{f}, \tag{3}$$

in which f_1 is the focal length of the concave mirror, f_2 is the focal length of the convex mirror and f_f is the focal length of the focusing lens.

Fig. 2 shows the integration of the beam shaping system with the focusing optics. A Yb:YAG laser source (TruDisk 10001, TRUMPF SE + Co. KG, Germany) with a beam parameter product (BPP) of $\frac{1}{4}d_0\theta_0 = 4$ mm mrad is employed. To maintain this beam quality, the laser light is transported from the laser source to the focusing optics via a ⌀100 μm optical transport fibre, in this case a 2-in-1 100/400 μm 2-in-1 fibre of which only the core is used. The fibre is coupled to the focusing optics (BEO D70), consisting of a collimator with focal length 150 mm, 90°dichroic mirror and focusing lens with focal length 600 mm. The dynamic beam shaping system (inside the rectangular box in Fig. 2) is integrated in the collimated beam path of the focusing optics, between the collimator and the dichroic mirror. The setup in this box consists of the Deformable Mirror (PDM30-37, Flexible Optical B.V., the Netherlands), a Galilean beam reducer comprising a concave and a convex mirror with focal lengths of 500 mm and −125 mm respectively, and two flat mirrors (3 fotonai, UAB, Lithuania). All these mirrors are coated with a high reflective coating (3 fotonai), having a reflectivity of >99.95% for the laser wavelength used in order to allow an optical power handling capacity up to 10 kW for the used mirrors. The DM is a 1.25 mm thick fused silica faceplate with a diameter of 30 mm which is illuminated by the collimated beam with a diameter of 24 mm (according to Eq. (2)) and a uniform intensity distribution as schematically shown in Fig. 3. To the backside of the mirror 37 piezoelectric actuators are bonded in a triangular pattern, the maximum stroke of the actuators is −6 μm at a voltage of 300 V. The DM is controlled using a ethernet control unit (EDAC-40, Flexible Optical) and a 40-channel High Voltage amplifier (Flexible Optical).

2.2. Analysis tools

Laser intensity profiles are analysed at both low and high laser power levels. Fig. 4(a) shows schematically the setup used for the low power measurements. It consists of the beam shaping optics and a CCD beam profiler (BC106-VIS, Thorlabs Inc., USA), which was positioned in the focal plane. Furthermore two neutral density filters (NG1 3 mm, Schott AG, Germany and NE30A-B, Thorlabs Inc., USA) are applied to attenuate the laser power to avoid damage and saturation of the CCD chip.

At high laser power levels, the laser beam is analysed using a scanning device comprising a rotating measurement tip, known as a focus monitor (FM, Primes GmbH, Germany), combined with a power monitor (PM 48, Primes GmbH, Germany), as schematically shown in Fig. 4(b). Unlike the CCD chip used at low power levels, the FocusMonitor is able to measure the PDD at different planes along the optical axis of the focused laser beam.

3. Method

In this section, the mathematical procedure is introduced and discussed to relate the desired beam shapes to actuator inputs of the DM. First, Section 3.1 shows the relation between the mirror surface and induced PDD based on a mathematical framework, which was introduced in our earlier work [27]. Next, in Section 3.2 the initial shape of the DM surface is addressed and it is discussed how this initial shape has to be incorporated in the mirror actuation procedure. Subsequently the relation between mirror surface and actuator input is explained in Section 3.3. Then, Section 3.4 introduces the six exemplary beam shapes and corresponding mirror surfaces. Finally, Section 3.5 describes the simulation of the resulting PDDs using the derived mirror surfaces and introduces the measure, i.e. a criterion, to compare simulated and measured PDDs.

3.1. DM surface - PDD relation

The adaptation of the PDD in the focal plane is dictated by the mirror surface elevation $M(x, y)$ of the DM. When the mirror surface is flat (i.e. $M(x, y) = 0$), it will not affect the PDD. In case the mirror surface is curved, the mirror will redistribute the laser irradiation and therefore

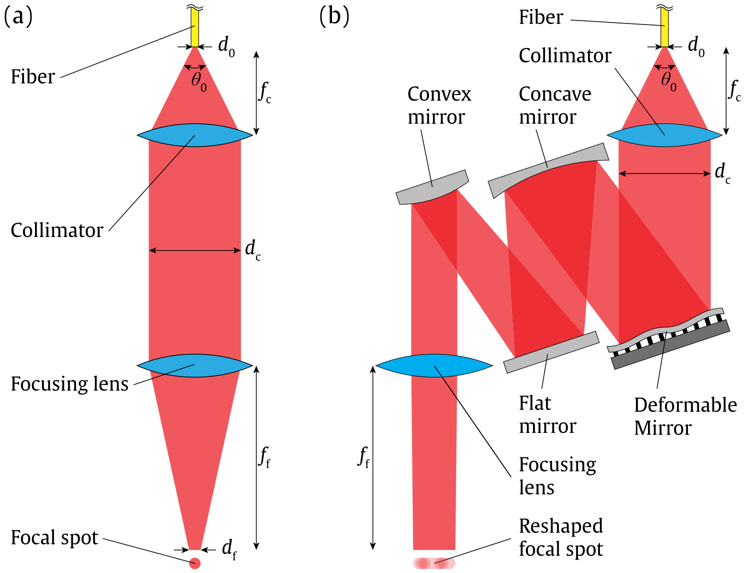

Fig. 1. Schematic overview optical layouts of (a) conventional setup and (b) dynamic beam shaping system including a DM and Galilean beam reducer (concave and convex mirrors).

shape the laser beam in the focal plane. A laser beamlet incident on the mirror at location $(x_{\mathrm{M}}, y_{\mathrm{M}})$ will be deflected with an angle which is twice the local angle of the mirror, i.e. the gradient of the mirror surface $\frac{\partial M}{\partial x}\left(x_{\mathrm{M}}, y_{\mathrm{M}}\right), \frac{\partial M}{\partial y}\left(x_{\mathrm{M}}, y_{\mathrm{M}}\right)$, as schematically shown (in 2D) in Fig. 5(a). Due to the deflection of the beamlet, the intersection point between the beamlet and the focal plane will change as schematically shown (in 2D) in Fig. 5(b). This changed intersection point $(x_{\mathrm{DM}}, y_{\mathrm{DM}})$ between the beamlet and the focal plane, shown in Fig. 5(c), is determined by the angle of deflection multiplied by the equivalent focal length f_{eq}, reading

$$x_{\mathrm{DM}}(x_{\mathrm{M}}, y_{\mathrm{M}}) = -2 f_{\mathrm{eq}} \frac{\partial M}{\partial x}(x_{\mathrm{M}}, y_{\mathrm{M}}), \tag{4}$$

$$y_{\mathrm{DM}}(x_{\mathrm{M}}, y_{\mathrm{M}}) = -2 f_{\mathrm{eq}} \frac{\partial M}{\partial y}(x_{\mathrm{M}}, y_{\mathrm{M}}). \tag{5}$$

The distribution of the intersection points between the beamlets and the focal plane determines the shaped PDD in this focal plane. In our earlier work [27], this distribution was referred to as the shape function $S(x, y)$ and defined as

$$S(x, y) = \frac{1}{A_{\mathrm{c}}} \iint_{A_{\mathrm{c}}} \delta\left(x - x_{\mathrm{DM}}(x_{\mathrm{M}}, y_{\mathrm{M}})\right) \delta\left(y - y_{\mathrm{DM}}(x_{\mathrm{M}}, y_{\mathrm{M}})\right) dx_{\mathrm{M}}\, dy_{\mathrm{M}}, \tag{6}$$

where δ is the Dirac delta function. A_{c} is the area of the mirror which is illuminated by the laser beam incident on the mirror, as shown in Fig. 3.

The PDD in the focal plane $I_{\mathrm{S}}(x, y)$ is subsequently mathematically computed by convolution of the unshaped PDD in the focal plane $I_{\mathrm{U}}(x, y)$ with this shape function $S(x, y)$ [27].

$$\begin{aligned} I_{\mathrm{S}}(x, y) &= I_{\mathrm{U}}(x, y) * S(x, y) \\ &= \iint_{A_S} I_{\mathrm{U}}(x - x', y - y') S(x', y')\, dx'\, dy', \end{aligned} \tag{7}$$

with A_{S} the shape function space. This shape function space is the area where I_{S} can exist, and therefore determined by the possible intersection points x_{DM} and y_{DM} of the beamlets with the focal plane as indicated in Fig. 5(c).

The mirror surface can be defined in a convex and a concave mode, as only the distribution of mirror surface *gradients* $\frac{\partial M}{\partial x}, \frac{\partial M}{\partial y}$ determine the shaped beam profile I_{S}. Therefore, for a given mirror surface M there is generally a second mirror surface M', defined as

$$M'(x_{\mathrm{M}}, y_{\mathrm{M}}) = -M(-x_{\mathrm{M}}, -y_{\mathrm{M}}), \tag{8}$$

inducing the same PDD I_{S}. This only holds for non-odd mirror surfaces M (i.e. $-M(-x_{\mathrm{M}}, -y_{\mathrm{M}}) \neq M(x_{\mathrm{M}}, y_{\mathrm{M}})$) as otherwise M and M' would be identical. Eq. (8) transforms a convex mirror surface in a concave one, or vice versa.

3.2. Compensation for unactuated non-flatness

Due to stresses induced by the applied optical coating and the assembly process, the initial mirror surface – i.e. the mirror surface without actuation of the piezo actuators – is not flat. This initial deformation has been measured by the mirror supplier and is shown in Fig. 6. As this unactuated non-flatness is in the same range as the required actuator strokes (see Section 2.1), it should be compensated for.

As actuating the DM will deform the DM with respect to this initial mirror surface, the mirror surface should be actuated based on a mirror surface $M_{\mathrm{act,in}}$ which is corrected for the initial mirror surface M_{init}. For this correction the initial mirror surface M_{init} is subtracted from the required mirror surface M_{req}, reading

$$M_{\mathrm{act,in}} = M_{\mathrm{req}} - M_{\mathrm{init}}. \tag{9}$$

As this initial mirror surface M_{init} is convex, it is convenient to define the required mirror surfaces are also in a convex mode, such that the DM has to deform less compared to the case with a flat initial mirror surface.

3.3. Mirror actuation

The DM surface is deformed by 37 piezo actuators, which are mounted in a triangular pattern on the backside of the mirror, as shown in Fig. 3. The mirror surface M is a linear combination of the actuator base functions M_i $(i = 1 \ldots 37)$. The base function M_i is the mirror surface when only the ith actuator is actuated at a voltage of $v_i = 1\mathrm{V}$. As examples, Fig. 7 shows four of these base functions, namely M_1, M_2, M_8 and M_{20}. The actuated mirror surface $M_{\mathrm{act,out}}$ is subsequently calculated with

$$M_{\mathrm{act,out}} = \sum_{i=1}^{37} v_i M_i, \tag{10}$$

in which v_i can be set by the user. These voltages v_i are calculated using the MrFit software, delivered by the DM supplier, which based on

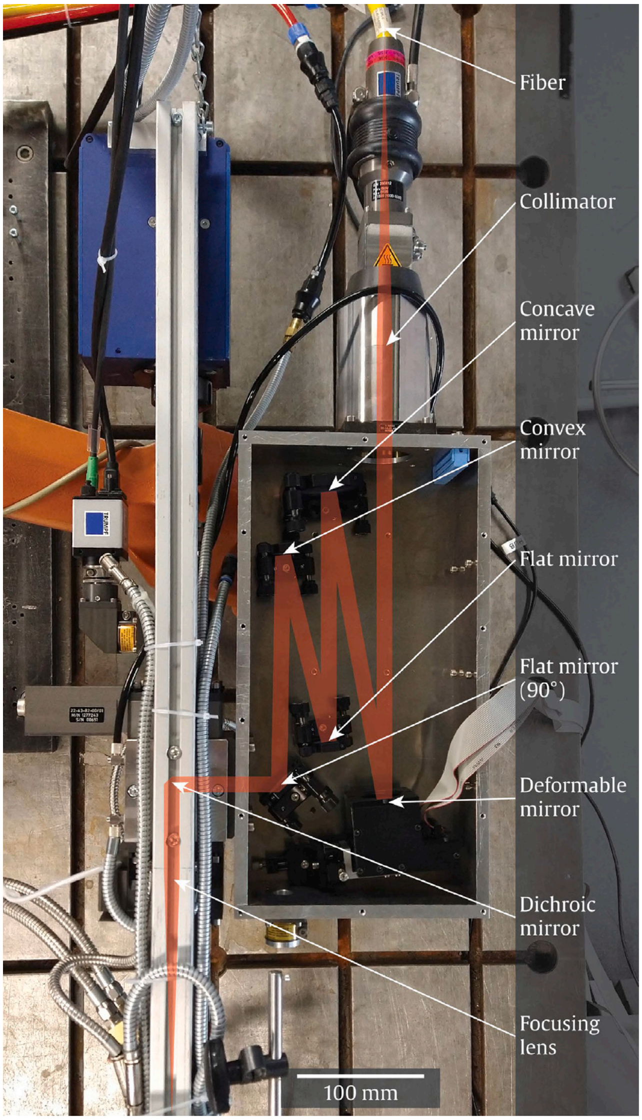

Fig. 2. Schematic overview optical layout of dynamic beam shaping system including a DM.

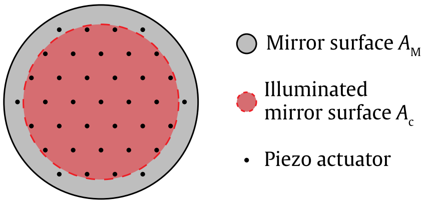

Fig. 3. Overview DM with mirror surface A_M, mirror surface A_c illuminated by the collimated laser beam incident on the mirror and locations (dots) of the attached piezo actuators at the backside of the mirror.

an algorithm minimises $M_{\mathrm{act,out}} - M_{\mathrm{act,in}}$. Subsequently the calculated voltages are fed to the mirror controller. The obtained mirror surface M_{obt} reads

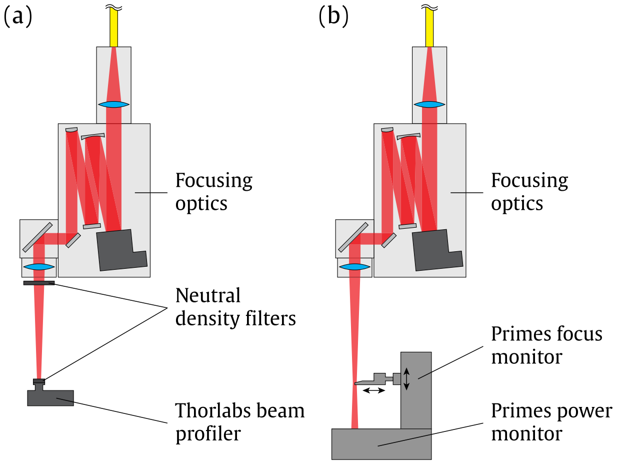

Fig. 4. Schematic overview measurement setups during (a) low power beam measurements and (b) high power beam measurements.

$$M_{\mathrm{obt}} = \sum_{i=1}^{37} v_i M_i + M_{\mathrm{init}}. \tag{11}$$

3.4. *Examples of beam shapes and corresponding mirror shapes*

This section defines several desired beam shapes and the corresponding required mirror surfaces M_{req}. These will depend on three parameters, the size of the beam shape $w = 3$ mm, the equivalent focal length $f_{\mathrm{eq}} = 2400$ mm (using Eq. (3) and focal lengths specified in Section 2.1) and the radius of the collimated beam $r_{\mathrm{c}} = d_{\mathrm{c}}/2 = 12$ mm (using Eq. (2) and the optical parameters specified in Section 2.1). The mirror surfaces will be defined in convex mode, which is convenient as mentioned in Section 3.2.

3.4.1. *Splitting beam in N identical laser spots*

The shape function S_{split} corresponding to splitting the incident laser beam into N laser spots, equally distributed over a circle (in the focal plane) with diameter w reads

$$S_{\mathrm{split}}(x, y) = \frac{1}{N}\sum_{n=1}^{N} \delta\left(x - \frac{w}{2}\cos(\varphi_n)\right)\delta\left(y - \frac{w}{2}\sin(\varphi_n)\right), \tag{12}$$

where $\varphi_n = 2\pi(n-1)/N + \varphi_0$. Fig. 8(a) shows this shape function schematically for the case $N = 3$ and $\varphi_0 = -\pi/3$.

As this shape function represents the distribution of the DM induced beamlet displacements $(x_{\mathrm{DM}}, y_{\mathrm{DM}})$ (see Eq. (6)), and these beamlet displacements are coupled to the mirror gradients $(\frac{\partial M_{\mathrm{req}}^{\mathrm{split}}}{\partial x}, \frac{\partial M_{\mathrm{req}}^{\mathrm{split}}}{\partial y})$ through Eqs. (4) and (5), it follows that the corresponding mirror surface should be divided in N sections with different constant gradients. These gradients read

$$\left(\frac{\partial M_{\mathrm{req}}^{\mathrm{split}}}{\partial x}, \frac{\partial M_{\mathrm{req}}^{\mathrm{split}}}{\partial y}\right)_n = \left(-\frac{w}{4f_{\mathrm{eq}}}\cos(\varphi_n), -\frac{w}{4f_{\mathrm{eq}}}\sin(\varphi_n)\right), \tag{13}$$

for $n \in 1, \ldots, N$. The corresponding mirror sections, if $N = 3$, are schematically shown in Fig. 8(b), where the boundaries between parts of the mirror surface are chosen in such a way that a continuous mirror surface $M_{\mathrm{req}}^{\mathrm{split}}$ is obtained. This required mirror surface is described by

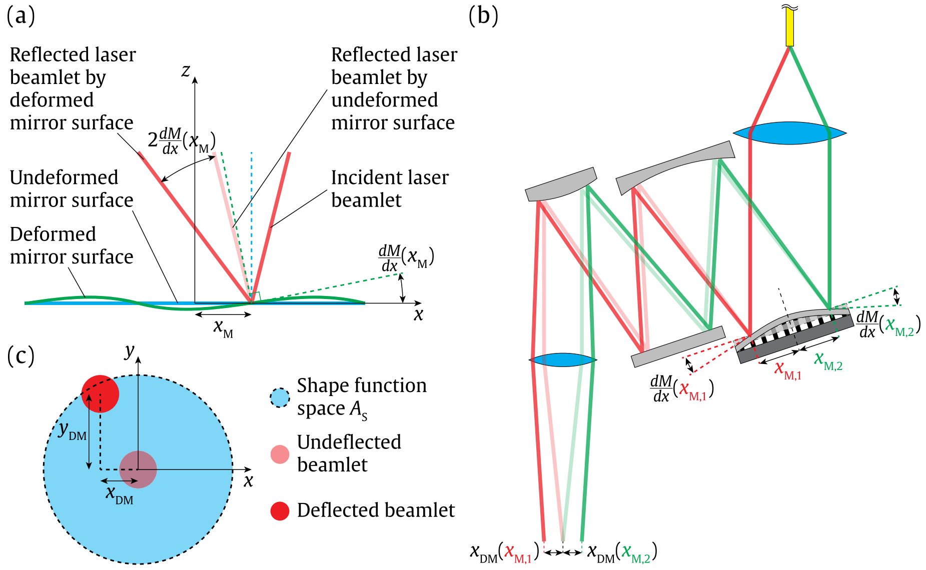

Fig. 5. Schematic overview of beamlet deflections at different locations and scales: (a) 2D representation of beamlet deflection at DM surface, (b) 2D representation of two beamlets along the beam path and (c) change of intersection point between the beamlet and the focal plane by beamlet deflection.

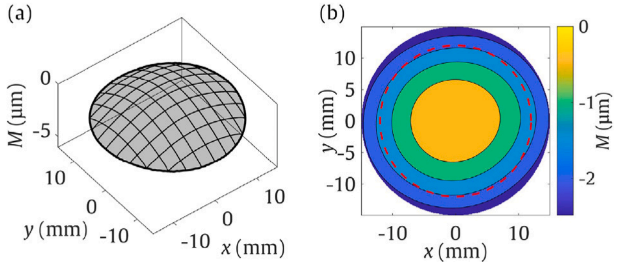

Fig. 6. (a) Isometric view and (b) contour plot of initial shape M_{init} of DM surface.

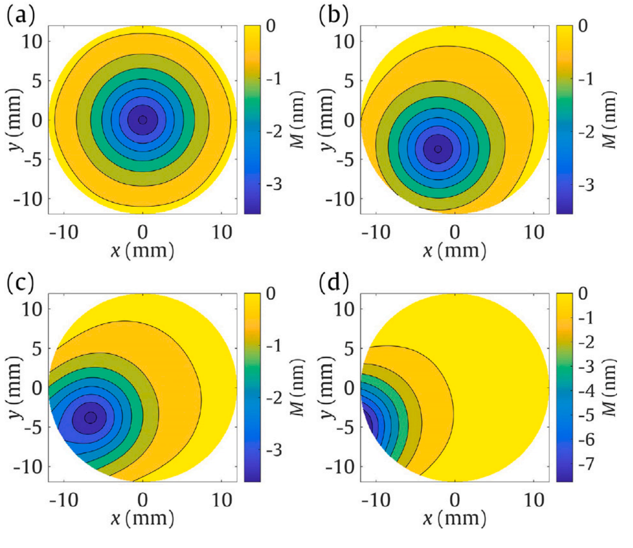

Fig. 7. Piezo actuator base functions (a) M_1, (b) M_2, (c) M_8 and (d) M_{20}.

$$M_{\text{req}}^{\text{split}}(x,y) = \begin{cases} \frac{w}{4f_{\text{eq}}}\left(-\frac{1}{2}x + \frac{\sqrt{3}}{2}y\right), & -\frac{2\pi}{3} < \varphi \le 0 \\ \frac{w}{4f_{\text{eq}}}\left(-\frac{1}{2}x - \frac{\sqrt{3}}{2}y\right), & 0 < \varphi \le \frac{2\pi}{3} \\ \frac{w}{4f_{\text{eq}}}x, & \frac{2\pi}{3} < \varphi \le \frac{4\pi}{3} \end{cases} \tag{14}$$

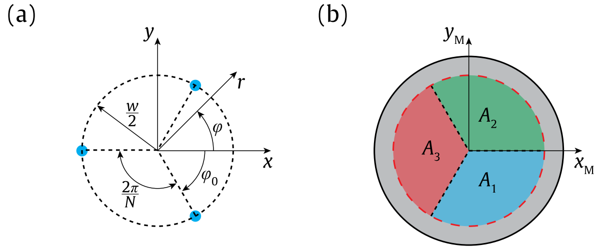

Fig. 8. Splitting the incident beam into $N = 3$ beams equally divided over a circle with a DM: (a) Shape function S_{split} in which the blue dots represent the locations of the laser spots and (b) schematic overview mirror surface $M_{\text{req}}^{\text{split}}$, corresponding to split .

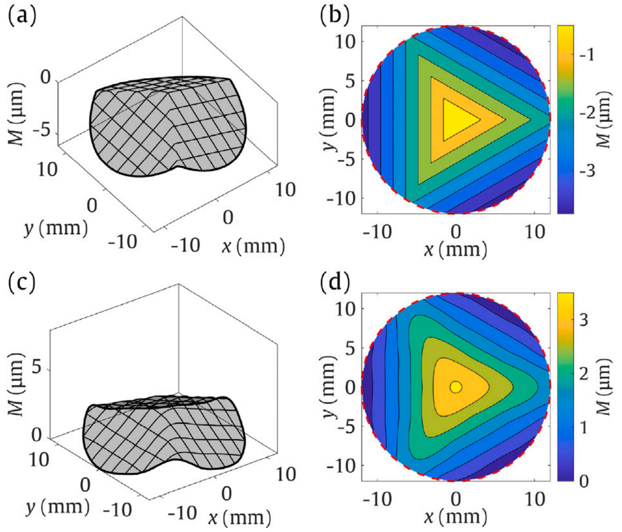

Fig. 9. (a), (c) Isometric view and (b), (d) contour plot of (a), (b) required and (c), (d) obtained DM surface to create PDD consisting out of three spots.

and shown, with w and f_{eq} as specified in Section 3.4, in Fig. 9(a) and (b). In this mirror surface three sharp edges are visible, which are unfeasible because the curvature of the mirror surface is limited

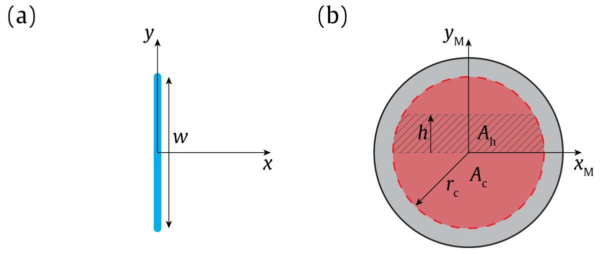

Fig. 10. Creating a line shaped PDD with a DM: (a) Shape function S_{line} and (b) schematic overview mirror surface $M^{\mathrm{line}}_{\mathrm{req}}$.

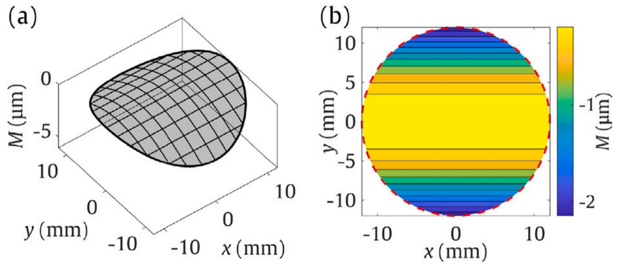

Fig. 11. (a) Isometric view and (b) contour plot of DM surface corresponding to a line shaped PDD.

in practice. When this mirror surface is corrected for the initial mirror surface (see Section 3.2), the required actuator voltages are computed and the mirror surface is calculated according to Eq. (11), the mirror surface of Fig. 9(c) and (d) is obtained. As can be concluded from these figure, in this mirror surface the unfeasible sharp edges disappeared and a smooth surface is obtained.

3.4.2. Line profile

The shape function S_{line} corresponding to a line shaped PDD reads

$$S_{\mathrm{line}}(x,y)=\tfrac{1}{w}\delta(x), \quad \text{if } -\tfrac{w}{2}<y<\tfrac{w}{2}, \tag{15}$$

where w is the length of the line. Fig. 10(a) shows this shape function S_{line}.

By comparing Eq. (15) to Eq. (6) it follows that $x_{\mathrm{DM}}(x_{\mathrm{M}},y_{\mathrm{M}})=0$ and values of $y_{\mathrm{DM}}(x_{\mathrm{M}},y_{\mathrm{M}})$ are uniformly distributed between $-\frac{w}{2}$ an $\frac{w}{2}$. Subsequently using Eqs. (4) and (5) shows that the x-component of the mirror surface gradients $\frac{\partial M^{\mathrm{line}}_{\mathrm{req}}}{\partial x}(x_{\mathrm{M}},y_{\mathrm{M}})=0$ and the y-component of the mirror surface gradients $\frac{\partial M^{\mathrm{line}}_{\mathrm{req}}}{\partial y}(x_{\mathrm{M}},y_{\mathrm{M}})$ is uniformly distributed between $-\frac{w}{4f_{\mathrm{eq}}}$ and $\frac{w}{4f_{\mathrm{eq}}}$. As the x-component of the mirror surface gradient $\frac{\partial M^{\mathrm{line}}_{\mathrm{req}}}{\partial x}=0$, the mirror surface M and thus the y-component of the mirror surface gradient $\frac{\partial M^{\mathrm{line}}_{\mathrm{req}}}{\partial y}$ are functions of y_{M} only. To create the uniform distribution of these gradients, the gradient at $y_{\mathrm{M}}=h$ is defined as

$$\frac{\partial M^{\mathrm{line}}_{\mathrm{req}}}{\partial y}=-\frac{2A_{\mathrm{h}}(h)}{A_{\mathrm{M}}}\frac{w}{4f_{\mathrm{eq}}}, \tag{16}$$

where A_{h} is the area of the mirror between the lines $y_{\mathrm{M}}=0$ and $y_{\mathrm{M}}=h$ illuminated by the incident laser beam, as schematically shown in Fig. 10(b). This area A_{h} follows from

$$\begin{aligned} A_{\mathrm{h}}(h) &= \int_0^h 2\sqrt{r_{\mathrm{c}}^2-y^2}\,dy \\ &= h\sqrt{r_{\mathrm{c}}^2-h^2}+r_{\mathrm{c}}^2\arctan\frac{h}{\sqrt{r_{\mathrm{c}}^2-h^2}}, \end{aligned} \tag{17}$$

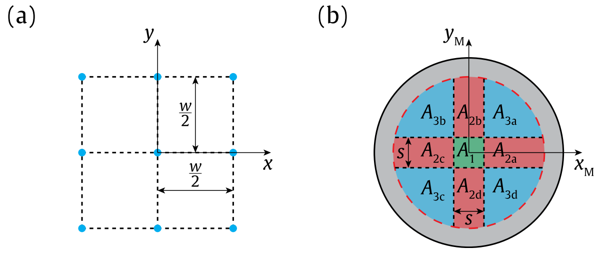

Fig. 12. Creating a square-like uniform PDD with a DM: (a) Shape function S_{sq} and (b) schematic overview mirror surface $M^{\mathrm{sq}}_{\mathrm{req}}$.

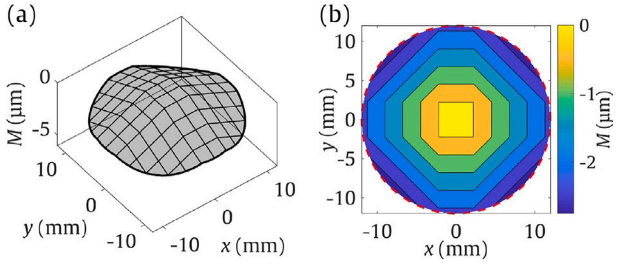

Fig. 13. (a) Isometric view and (b) contour plot of DM surface corresponding to a square-like uniform PDD.

where r_{c} is the radius of the illuminated mirror surface A_{c}. When combining Eqs. (16) and (17) and using $A_{\mathrm{c}}=\pi r_{\mathrm{c}}^2$ gives

$$\frac{\partial M^{\mathrm{line}}_{\mathrm{req}}}{\partial y}=-\frac{w}{4f_{\mathrm{eq}}}\frac{2}{\pi r_{\mathrm{c}}^2}\left(x\sqrt{r_{\mathrm{c}}^2-y^2}+r_{\mathrm{c}}^2\arctan\frac{y}{\sqrt{r_{\mathrm{c}}^2-y^2}}\right). \tag{18}$$

Integrating this expression over y using the boundary condition $M^{\mathrm{line}}_{\mathrm{req}}(y=0)=0$, an expression for the mirror surface $M^{\mathrm{line}}_{\mathrm{req}}$ is obtained, which reads

$$\begin{aligned} M^{\mathrm{line}}_{\mathrm{req}} = -\frac{w}{4f_{\mathrm{eq}}}\frac{2}{\pi r_{\mathrm{c}}^2}\Bigg(&\frac{1}{3}\sqrt{r_{\mathrm{c}}^2-y^2}(2r_{\mathrm{c}}^2+y^2) \\ &+r_{\mathrm{c}}^2 y\arctan\frac{y}{\sqrt{r_{\mathrm{c}}^2-y^2}}-\frac{2}{3}r_{\mathrm{c}}^3\Bigg). \end{aligned} \tag{19}$$

Fig. 11 illustrates this mirror surface when the parameters w, f_{eq} and r_{c} as specified in Section 3.4 are used.

3.4.3. Square uniform profile

A square-like uniform PDD can be approached by splitting the incident laser beam into 9 spots, ordered in a 3×3 grid as schematically shown in Fig. 12(a). The corresponding shape function S_{sq} reads

$$\begin{aligned} S_{\mathrm{sq}}(x,y) &= a_1\delta(x)\delta(y) \\ &+a_2\left(\delta(x)\delta\left(|y|-\frac{w}{2}\right)+\delta\left(|x|-\frac{w}{2}\right)\delta(y)\right) \\ &+a_3\delta\left(|x|-\frac{w}{2}\right)\delta\left(|y|-\frac{w}{2}\right), \end{aligned} \tag{20}$$

where a_1, a_2 and a_3 define the laser power distribution between the different spots, i.e. $a_1+4a_2+4a_3=1$. When comparing this equation to Eq. (6) and using Eqs. (4) and (5) it follows that the mirror surface should be divided into 9 mirror sections characterised by $\frac{\partial M^{\mathrm{sq}}_{\mathrm{req}}}{\partial x}=-\frac{w}{4f_{\mathrm{eq}}}$, $\frac{\partial M^{\mathrm{sq}}_{\mathrm{req}}}{\partial x}=0$ or $\frac{\partial M^{\mathrm{sq}}_{\mathrm{req}}}{\partial x}=\frac{w}{4f_{\mathrm{eq}}}$ and $\frac{\partial M^{\mathrm{sq}}_{\mathrm{req}}}{\partial y}=-\frac{w}{4f_{\mathrm{eq}}}$, $\frac{\partial M^{\mathrm{sq}}_{\mathrm{req}}}{\partial y}=0$ or $\frac{\partial M^{\mathrm{sq}}_{\mathrm{req}}}{\partial y}=\frac{w}{4f_{\mathrm{eq}}}$. These 9 mirror sections are schematically shown in Fig. 12(b).

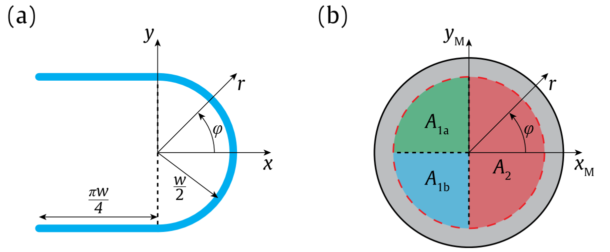

Fig. 14. Creating a horseshoe PDD with a DM: (a) Shape function S_{hs} and (b) schematic overview mirror surface $M_{\mathrm{req}}^{\mathrm{hs}}$.

The surface section area sizes relative to the mirror surface area A_{c} illuminated by the incident laser beam are

$$\frac{A_1}{A_c} = a_1, \tag{21}$$

$$\frac{A_{2a}}{A_c} = \frac{A_{2b}}{A_c} = \frac{A_{2c}}{A_c} = \frac{A_{2d}}{A_c} = a_2, \tag{22}$$

$$\frac{A_{3a}}{A_c} = \frac{A_{3b}}{A_c} = \frac{A_{3c}}{A_c} = \frac{A_{3d}}{A_c} = a_3, \tag{23}$$

and the corresponding mirror surface equals

$$M_{\mathrm{req}}^{\mathrm{sq}}(x,y) = \begin{cases} 0, & |x| \le \frac{s}{2},\ |y| \le \frac{s}{2} \\ -\frac{w}{4f_{\mathrm{eq}}}\left(|x| - \frac{s}{2}\right), & |x| > \frac{s}{2},\ |y| \le \frac{s}{2} \\ -\frac{w}{4f_{\mathrm{eq}}}\left(|y| - \frac{s}{2}\right), & |x| \le \frac{s}{2},\ |y| > \frac{s}{2} \\ -\frac{w}{4f_{\mathrm{eq}}}\left(|x| + |y| - s\right), & |x| > \frac{s}{2},\ |y| > \frac{s}{2} \end{cases} \tag{24}$$

in which s is defined in Fig. 12(b). In the case $s = 4.5$ mm this results in $a_1 \approx 0.04$, $a_2 \approx 0.1$ and $a_3 \approx 0.14$. Fig. 13 shows the resulting mirror surface shape using w and f_{eq} as defined in Section 3.4.

3.4.4. Horseshoe profile

The shape function S_{hs} corresponding to a horseshoe shaped PDD consists out of a semicircle with diameter w and two horizontal line segments at the edges of the semi circle and defined as

$$S_{\mathrm{hs}}(x,y) = \begin{cases} \frac{1}{\pi w}\delta\left(x - \frac{w}{2}\cos(\varphi)\right)\delta\left(y - \frac{w}{2}\sin(\varphi)\right), \\ \quad x \ge 0 \\ \frac{1}{\pi w}\delta\left(|y| - \frac{w}{2}\right), \\ \quad -\frac{\pi w}{4} \le x < 0 \end{cases} \tag{25}$$

where the length of each line segment is chosen equal to half the arc length of the semicircle, as shown in Fig. 14(a).

When comparing this shape function S_{hs} (Eq. (25)) to Eq. (6) it follows that half of the illuminated mirror surface A_{c} should be used for the semicircle and two times a quarter of A_{c} should be used to for each of the line segments, see Fig. 14(b). In this figure, the right half of the mirror surface A_2 corresponds to the semicircle and the upper and lower left quarters of the mirror surface ($A_{1\mathrm{a}}$ and $A_{1\mathrm{b}}$) correspond to, respectively, the upper and lower line segments of the shape function S_{hs}.

When using Eqs. ((6), (4) and (5)) for the semicircle part of the shape function (upper expression of Eq. (25)), it follows for the mirror gradients that

$$-2f_{\mathrm{eq}}\frac{\partial M_{\mathrm{req}}^{\mathrm{hs}}}{\partial x} = \frac{w}{2}\cos(\varphi), \tag{26}$$

$$-2f_{\mathrm{eq}}\frac{\partial M_{\mathrm{req}}^{\mathrm{hs}}}{\partial y} = \frac{w}{2}\sin(\varphi), \quad |\varphi| \le \frac{\pi}{2}. \tag{27}$$

These equations can be expressed in the gradient of the mirror surface in radial direction $\frac{\partial M_{\mathrm{req}}^{\mathrm{hs}}}{\partial r}$ using

$$\frac{\partial M_{\mathrm{req}}^{\mathrm{hs}}}{\partial r} = \frac{\partial M_{\mathrm{req}}^{\mathrm{hs}}}{\partial x}\cos(\varphi) + \frac{\partial M_{\mathrm{req}}^{\mathrm{hs}}}{\partial y}\sin(\varphi). \tag{28}$$

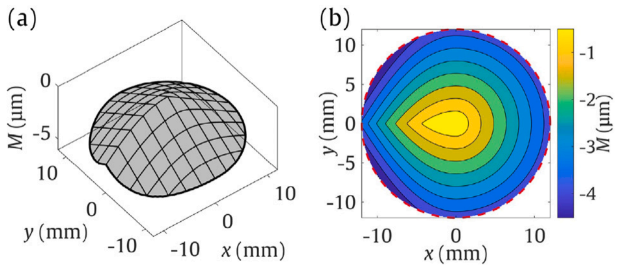

Fig. 15. (a) Isometric view and (b) contour plot of DM surface corresponding to a horseshoe PDD.

Substituting Eqs. (26) and (27) into Eq. (28) yields

$$\begin{aligned} \frac{\partial M_{\mathrm{req}}^{\mathrm{hs}}}{\partial r} &= -\frac{w}{4f_{\mathrm{eq}}}\cos^2(\varphi) - \frac{w}{4f_{\mathrm{eq}}}\sin^2(\varphi) \\ &= -\frac{w}{4f_{\mathrm{eq}}}, \quad |\varphi| \le \frac{\pi}{2}, \end{aligned} \tag{29}$$

which leads to the mirror surface defined by

$$M_{\mathrm{req}}^{\mathrm{hs}} = -\frac{wr}{4f_{\mathrm{eq}}}, \quad |\varphi| \le \frac{\pi}{2}. \tag{30}$$

Then, when comparing the second expression of Eqs. (25) to (6) and subsequently using Eqs. (4) and (5) it follows that for the upper and lower line segments the y-components of the surface gradients equal $\frac{\partial M_{\mathrm{req}}^{\mathrm{hs}}}{\partial y} = -\frac{w}{4f_{\mathrm{eq}}}$ and $\frac{\partial M_{\mathrm{req}}^{\mathrm{hs}}}{\partial y} = \frac{w}{4f_{\mathrm{eq}}}$, respectively, and the x-components of the surface gradients are uniformly distributed between $\frac{\pi w}{4}$ and 0. For the latter the same procedure as for the line-shaped laser intensity profile in Section 3.4.2, that is, Eqs. (16) through (19) are followed, but in the x-direction instead of in the y-direction. This results for mirror surface section $A_{1\mathrm{a}}$ in

$$M_{\mathrm{req}}^{\mathrm{hs}} = \frac{w}{4f_{\mathrm{eq}}}\left(-y + \frac{1}{r_c^2}\left(\frac{1}{3}\sqrt{r_{\mathrm{c}}^2 - x^2}(2r_{\mathrm{c}}^2 + x^2) + r_{\mathrm{c}}^2 x \arctan\frac{x}{\sqrt{r_{\mathrm{c}}^2 - x^2}}\right) - \frac{2}{3}r_{\mathrm{c}}\right), \tag{31}$$

and for mirror surface section $A_{1\mathrm{b}}$ in

$$M_{\mathrm{req}}^{\mathrm{hs}} = \frac{w}{4f_{\mathrm{eq}}}\left(y + \frac{1}{r_c^2}\left(\frac{1}{3}\sqrt{r_{\mathrm{c}}^2 - x^2}(2r_{\mathrm{c}}^2 + x^2) + r_{\mathrm{c}}^2 x \arctan\frac{x}{\sqrt{r_{\mathrm{c}}^2 - x^2}}\right) - \frac{2}{3}r_{\mathrm{c}}\right). \tag{32}$$

Combining the expressions for the three sections of the mirror surface, i.e. Eqs. (30), (31) and (32) yields

$$M_{\mathrm{req}}^{\mathrm{hs}}(x,y) = \begin{cases} \frac{rw}{4f_{\mathrm{eq}}}, & |\varphi| \ge \frac{\pi}{2} \\ \frac{w}{4f_{\mathrm{eq}}}\left(|y| + \frac{1}{r_c^2}\left(\frac{1}{3}\sqrt{r_{\mathrm{c}}^2 - x^2}(2r_{\mathrm{c}}^2 + x^2) + r_{\mathrm{c}}^2 x \arctan\frac{x}{\sqrt{r_{\mathrm{c}}^2 - x^2}}\right) - \frac{2}{3}r_{\mathrm{c}}\right), & |\varphi| < \frac{\pi}{2} \end{cases} \tag{33}$$

Fig. 15 illustrates this mirror surface for w, f_{eq} and r_{c} as specified in Section 3.4.

3.4.5. Variations of the horseshoe profile

This section presents and discusses variations of the shape function corresponding to the horsehoe as presented in the previous section,

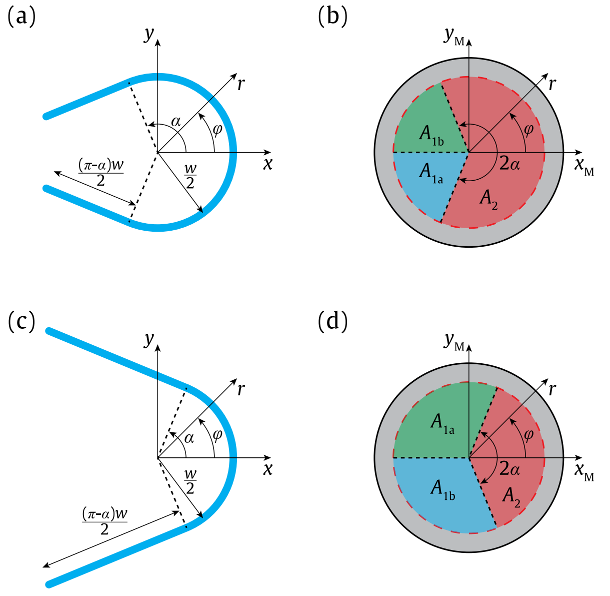

Fig. 16. Creating horseshoe PDDs with line segments (a), (b) inclined inwards and (c), (d) inclined outwards with a DM: (a), (c) Shape functions $S_{\mathrm{hs,in}}$ and $S_{\mathrm{hs,out}}$ and (b), (d) schematic overview mirror surfaces $M_{\mathrm{req}}^{\mathrm{hs,in}}$ and $M_{\mathrm{req}}^{\mathrm{hs,out}}$.

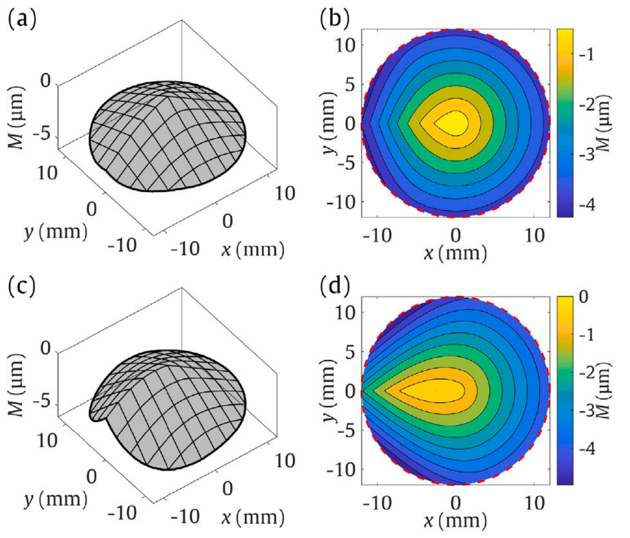

Fig. 17. (a), (c) Isometric view and (b), (d) contour plot of DM surfaces corresponding to horseshoe PDDs with line segments (a), (b) inclined inwards and (c), (d) inclined outwards.

namely a horseshoe profile in which the line segments are inclined inwards and a horseshoe profile in which the line segments are inclined outwards.

The horseshoe profile with inwards or outwards inclined line segments consists out of a circular arc subtending an angle of 2α (respectively larger or smaller than π) and two line segments with a length $w(\pi-\alpha)/2$, tangentially extended at the ends of the circular arc. Mathematically this shape function reads

$$S_{\mathrm{hs,var}}(x,y)=\begin{cases}\frac{1}{\pi w}\delta\left(x-\frac{w}{2}\cos(\varphi)\right)\delta\left(y-\frac{w}{2}\sin(\varphi)\right), \\ \quad x'\geq 0 \\ \frac{1}{\pi w}\delta\left(|y'|-\frac{w}{2}\right), \\ \quad -\frac{(\pi-\alpha)w}{2}\leq x'<0\end{cases} \tag{34}$$

where $x'=x\sin(\alpha)-|y|\cos(\alpha)$ and $|y'|=|y|\sin(\alpha)+x\cos(\alpha)$.

A change in length of the circular arc will require a change in the mirror surface section A_2 corresponding to this part of the shape function, which is schematically shown in Fig. 16. The corresponding mirror surface M is derived similar to the derivation of Eq. (33) which results in

$$M_{\mathrm{req}}^{\mathrm{hs,var}}(x,y)=\begin{cases}\frac{rw}{4f_{\mathrm{eq}}}, & |\varphi|\geq\pi-\alpha \\ \frac{w}{4f_{\mathrm{eq}}}\Bigg(|y'| & \\ \quad +\frac{1}{r_{\mathrm{c}}^{2}}\Bigg(\frac{1}{3}\sqrt{r_{\mathrm{c}}^{2}-x'^{2}}(2r_{\mathrm{c}}^{2}+x'^{2}) & \\ \quad +r_{\mathrm{c}}^{2}x'\arctan\frac{x'}{\sqrt{r_{\mathrm{c}}^{2}-x'^{2}}} & \\ \quad -\frac{1}{3}\tan(\alpha-\frac{\pi}{2})x'^{3}\Bigg)-\frac{2}{3}r_{\mathrm{c}}\Bigg), & |\varphi|<\pi-\alpha\end{cases} \tag{35}$$

Fig. 17(a) and (b) show the obtained mirror surface for the horseshoe profile with inwards inclined line segments ($\alpha=\frac{5}{8}\pi$) whereas 17(c) and (d) show the obtained mirror surface for the horseshoe profile with outwards inclined line segments.

3.5. Simulation and comparison PDDs

To obtain the mirror surfaces defined in the previous subsection, actuator voltages are calculated using the method as described in Section 3.3. Subsequently these obtained mirror surfaces M_{obt} are used to determine the obtained shape functions (applying Eqs. (4), (5) and (6)), which together with the unshaped laser intensity profile I_{U} (Fig. 18) is used to simulate the expected shaped laser intensity profiles, i.e. applying Eq. (7).

To quantify the performance of the beam shaping system, the similarity between the measured PDDs I_{M} and simulated PDDs I_{S} can be computed using the so-called overlapping index [28]. Complementary to this overlapping index, the error is defined here as

$$\mathrm{error}=100\%\cdot(1-\mathrm{overlap})=100\%\cdot\frac{1}{2P}\int_{A_{\mathrm{I}}}\left|I_{\mathrm{M}}-I_{\mathrm{S}}\right|\,dx\,dy, \tag{36}$$

where P is the applied laser power and A_{I} is the area in the focal plane where the measured and simulated PDDs are defined.

4. Results and discussion

This section presents and discusses experimental results of measured PPD's induced by the mirror surface derived in the previous section using the analysis tools presented in Section 2.2. First, in Section 4.1 the initial, unshaped PDD is discussed. Subsequently Section 4.2 presents the induced PDDs by the mirror surface shapes as defined in Section 3.4 at a relatively low laser power level (0.4 W). Lastly, Section 4.3 presents the effect of high(er) laser power levels (0.5 – 1 kW) on the mirror surface and resulting PDDs.

4.1. Initial unshaped PDD

In order to measure the PDD I_{U} of the initial, unshaped laser beam without aberrations induced by (initial) non-flatness of the unactuated DM surface (see Section 3.2), a flat mirror (PF10-03-P01, Thorlabs Inc., USA) was installed in the optical setup (see Figs. 1 and 2) instead of the DM. Fig. 18 shows the measured initial PDD I_{U} in the focal plane.

Fig. 19(a) shows the measured PDD I in the focal plane when the DM is installed, but not actuated. The difference between this PDD and the initial PDD I_{U} is shown in Fig. 19(b). This difference results in an error of 33.0% of the laser power. The error is computed using Eq. (36), here applied to the difference $I-I_{\mathrm{U}}$. It can be observed from Fig. 19(a) that the unactuated DM surface results in a PDD which is defocussed, when compared to I_{U}. This defocus is slightly more in the y-direction than in the x-direction, which is as expected, as the initial shape of the

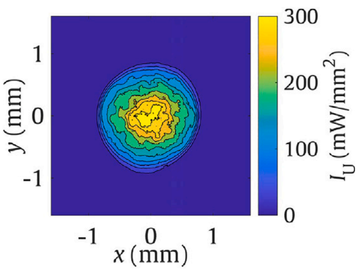

Fig. 18. PDD I_U in the focal plane when a flat mirror is installed in the optical setup instead of the DM.

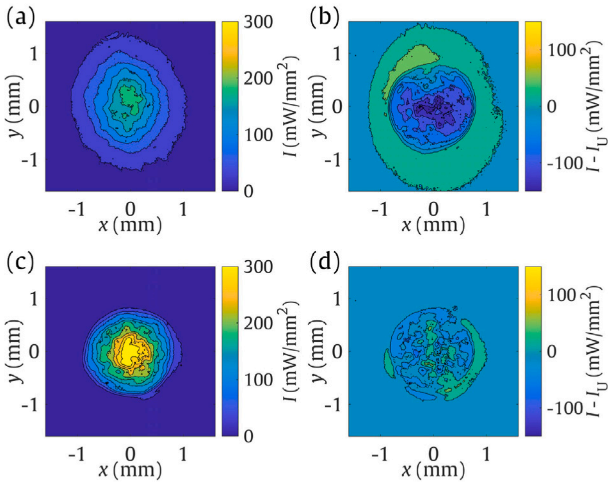

Fig. 19. (a), (c) Laser intensity profile of focal spot and (b), (d) difference with flat mirror (Fig. 18): (a), (b) unactuated DM and (c), (d) DM actuated to compensate initial mirror surface deformation.

mirror surface (Fig. 6) is also slightly more curved in y-direction than in x-direction. To compensate for this initial shape of the DM surface, the inverse of the initial shape is used to compute the actuator inputs ($M_{act,in} = -M_{\mathrm{init}}$, see Eq. (9)). As the mirror surface approximates a flat mirror surface in this case, the resulting PDD, shown in Fig. 19(c), is nearly equal to the initial PDD I_U, see Fig. 18. The difference is shown in Fig. 19(d), which results in an error of 7.7% of the total power.

4.2. Measured PDDs at low laser power levels

Using the procedure as described in Section 3.5, the six expected PDDs are simulated. These simulated PDDs I_S are shown in the left column of Fig. 20. The centre column of Fig. 20 shows the measured PDDs I_M using the low power measurement setup as explained in Section 2.2 and a average laser power of 0.4 W (pulsed mode, pulse length of 1 ms, pulse energy of 0.2 J and pulse rate 2 Hz). The right column shows the difference $I_M - I_S$ between the measured and simulated laser intensity profiles.

The measured laser intensity profile for the splitted beam profile in Fig. 20(b) shows in radial direction elliptical spots compared to the simulated profile of Fig. 20(b), which is attributed to the fact that the three surface sections of the mirror profile (see Figs. 8 and 9) are not flat, but slightly curved. From the difference $I_M - I_S$ in Fig. 20(c) it can be observed that the upper right spot is slightly translated. This induces difference values up to around 50% of the maximum intensities in Fig. 20(a) and (b), however the total error, computed using Eq. (36), is only 15% of the power.

For the line shaped beam profile, the measurements (Fig. 20(e)) show a wider beam in the centre of the line when compared to the simulation (Fig. 20(d)), which indicates that the mirror surface is also slightly curved in x-direction. The difference between the measured and simulated PDDs (Fig. 20(f)) results in a total error of 14.4% of the power.

Larger differences between the measurement and simulation are found for the square-like PDD. The four intensity peaks in the measured PDD of Fig. 20(h) are closer to the centre of the profile than in the simulated profile (in Fig. 20(g)) which implies that the actual mirror surface was flatter than the simulated surface. The difference between the measured and simulated PDDs is shown in Fig. 20(i), with a total error of 18.5%.

In contrast to the square-like PDD, the measured horseshoe PDD in Fig. 20(k) is slightly wider than the simulated PDD in Fig. 20(j). This is due to the gradients of the actual mirror surface corresponding to the horseshoe profile are somewhat steeper in radial direction than simulated. In turn, the length of the line segments is shorter than the length in the simulation. The difference between the two PDDs is shown in Fig. 20(l), which has a total error of 19.8%.

In Fig. 20(n) and (q) the measured intensity profiles for the horseshoe variations are shown. It can be observed that the line segments indeed inclined inwards and outwards, respectively, which match with the simulation results in Fig. 20(m) and (p). For the horseshoe with inwards inclined line segments, the width of the beam shape was somewhat closer to the simulated width. Indeed the difference between the measured and simulated profile shown in Fig. 20(m) is 14.2%, which is a bit smaller than for the standard horseshoe. For the horseshoe with outwards inclined line segments the differences between the measurement and simulation are shown in Fig. 20(r) with a total error of 19.4%, which is similar to the standard horseshoe.

4.3. Measured horseshoe PDD at high laser power levels

In this section the results and implications of using higher levels of power are presented and discussed. Measurements are performed using the high power measurement setup, as presented in Section 2.2. The in this section indicated power levels are the set power levels, the measured power levers were in all measurements up to 4% higher than the set power levels. Fig. 21(a) shows the obtained PDD for the horseshoe beam profile (Section 3.4.4) at 500 W. Although a horseshoe-like shaped PDD can be clearly identified, the PDD appears to be squeezed when compared to the low power measurement, see Fig. 20(k). This implies that the power of 500 W induces a reduction of the curvature of the DM and thus the mirror gradients. These mirror distortions are attributed to thermal stresses due to laser energy absorbed by the mirror, despite the fact that the reflectivity of DM surface is high (>99.95%). Yet, due to the relatively small thickness of the mirror (1.25 mm), even a small absorption of laser energy can thermally deform the mirror. The reduction of the gradients and therefore the change in mirror surface $M_{500\ \mathrm{W}}$ is approximated by a concave defocus as shown in Fig. 22.

This deformation of mirror surface due to a laser power of 500 W can be compensated similarly to the method used to compensate the initial unactuated mirror surface M_{init}. That is, Eq. (9) is extended to

$$M_{\mathrm{act,in}} = M_{\mathrm{req}} - M_{\mathrm{init}} - M_{500\ \mathrm{W}}, \tag{37}$$

which is subsequently used to determine the actuator voltages. This leads to the PDD of Fig. 21(b), which is again as desired and its size is similar to the profile at low laser power measurement (Fig. 20(k)). When increasing the power to 750 W and 1000 W while compensating for the 500 W mirror deformation, the PDDs of Fig. 23(a) and (b) are obtained, respectively. From these figures, it can be concluded that due to the increasing power the dimensions of the PDD decrease, indicating an increasing concave defocus. The latter distortions could be compensated by determining $M_{750\ \mathrm{W}}$ and $M_{1000\ \mathrm{W}}$. However, a more flexible approach would be to integrate a real time monitoring system which measures the wavefront of the reflected beam by the DM with a Shack–Hartmann wavefront sensor [23,29]. Then, using the

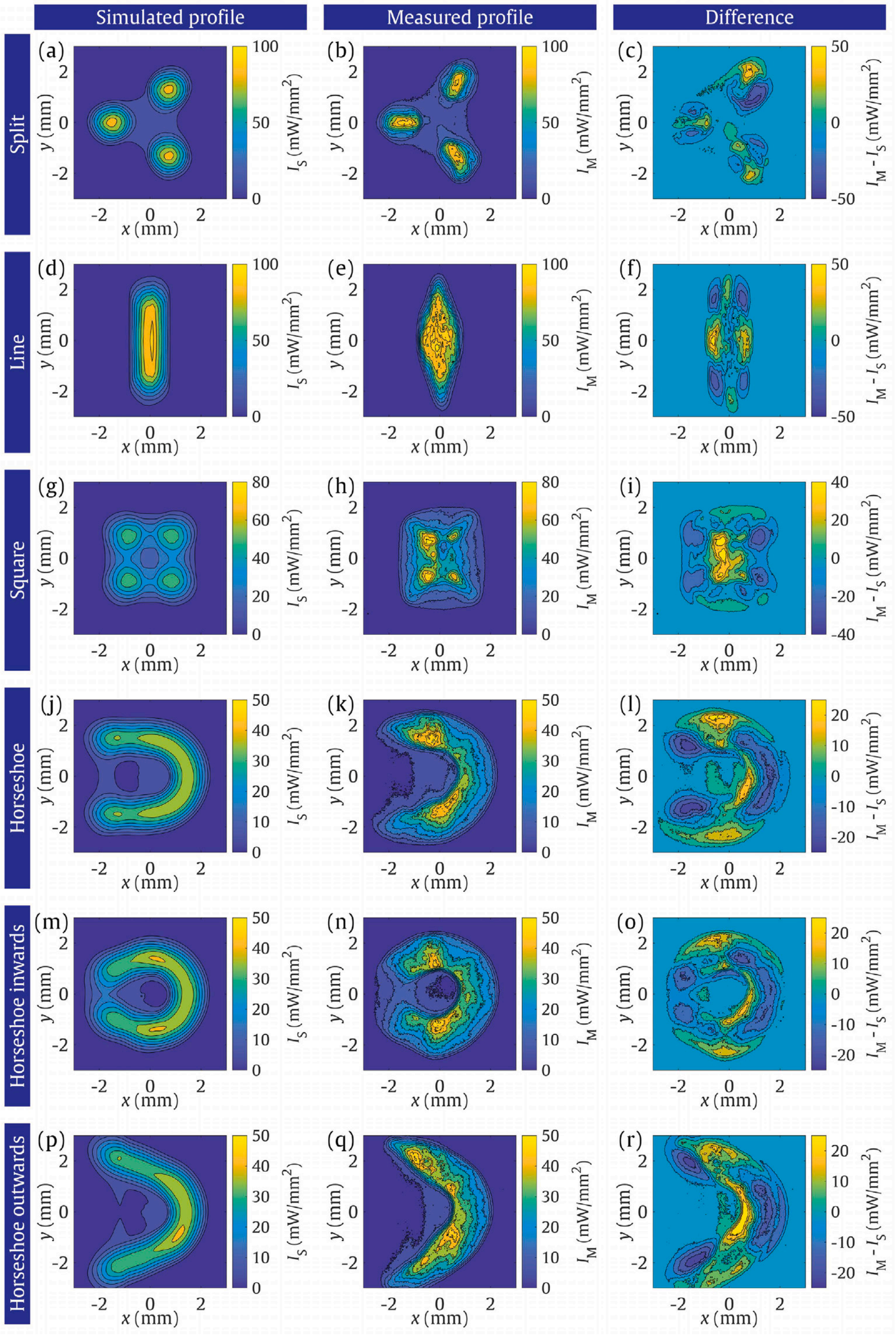

Fig. 20. Simulated (left column) and measured (central column) laser intensity profiles and their differences (right column) of the various PDDs.

sensor output, the actual mirror shape can be derived and closed loop control of the mirror actuation can account for dynamic errors in the mirror surface.

Furthermore, as the laser power related (concave) distortion increases with increasing laser power, the combination $M_{\text{init}} + M_{\text{xxxxW}}$ might result in the mirror surface become concave instead of convex. In the latter case it is beneficial to convert the concave desired mirror surfaces M_{req} to convex surfaces using Eq. (8).

When the horseshoe beam profile is measured at several planes above and below the focal plane, the laser intensity profiles of Fig. 24 are obtained. From this figure it can be concluded that in a large range from −100mm to +100 mm along the optical axis, the dimensions, width and length, of the profile only vary +14% and −9% respectively. Therefore, this optical design implies a large depth of focus. In laser material processes this allows to work in a range of working distances, without significantly changing the laser intensity profile.

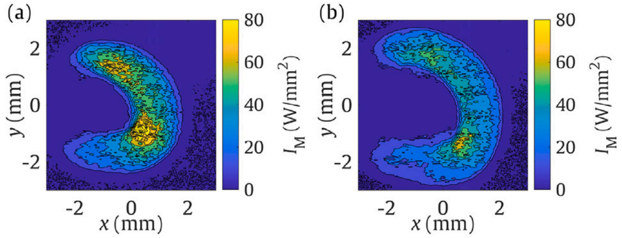

Fig. 21. Laser intensity profile of focal spot of horseshoe shaped beam with (a) mirror surface only compensated for initial mirror shape and (b) mirror surface compensated for initial mirror shape and thermal deformation at 500 W.

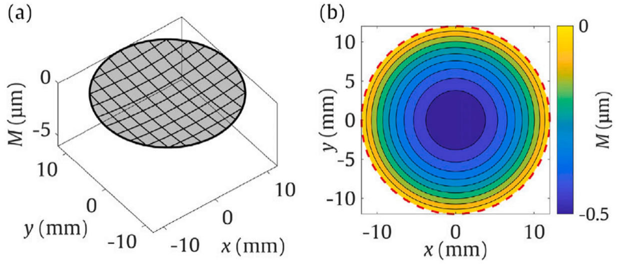

Fig. 22. (a) Isometric view and (b) contour plot of change in shape $M_{500\ \mathrm{W}}$ of DM surface induced by a laser power of 500 W.

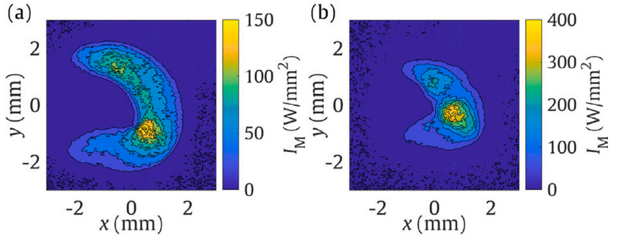

Fig. 23. Laser intensity profile of focal spot of horseshoe shaped beam mirror surface compensated for initial mirror shape and thermal deformation at 500 W and exposed at (a) 750 W and (b) 1000 W.

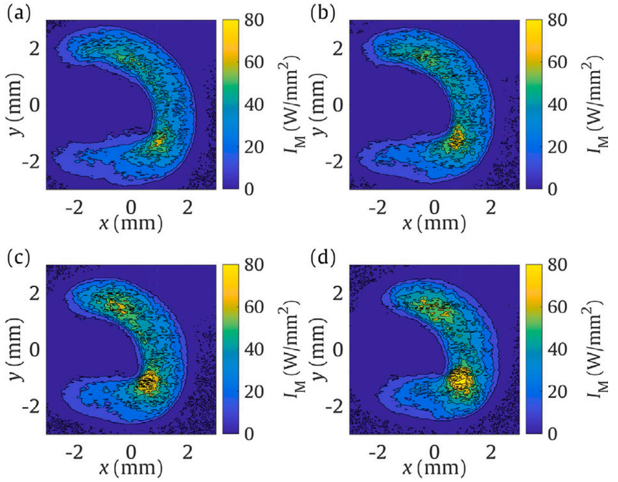

Fig. 24. Laser intensity profile of focal spot of horseshoe shaped beam with mirror surface compensated for initial mirror shape and thermal deformation at 500 W measured in planes at (a) −100 mm, (b) −50 mm, (c) +50 mm and (d) +100 mm distance from the focal plane.

5. Conclusions

In order to enable dynamic beam shaping during high power laser material processes an adaptive focusing optic based on a Deformable Mirror has been designed, implemented and evaluated. Using a mathematical framework, mirror surfaces corresponding to several significantly different laser intensity profiles were derived.

Simulations, based on the actuator inputs and actuator modes of the mirror surface show that the Deformable Mirror is able to approximate the desired mirror shapes.

At low laser power levels, measurements of the laser intensity profiles for the various beam shapes show a good agreement with the simulated profiles, based on the simulated mirror surfaces. Deviations between the measured and simulated profiles range between 14% and 20% of the laser power.

High laser power level measurements of the horseshoe shaped beam profile showed the ability of the beam shaping in handling high(er) laser powers. However, the increased laser power induced some additional (thermal) deformations of the mirror surface, which can be compensated by the mirror actuation. Therefore, integration of a sensor measuring the mirror and closed loop control with the mirror actuation is suggested to improve DM performance.

The obtained beam in the measured optical configuration showed a relatively large depth of focus. That is, over the measured range (±100 mm from focal plane) relatively small changes (<14%) in dimensions of the laser intensity profile are observed.

Therefore, the developed dynamic beam shaping system is a versatile tool to improve the adaptability of various laser processes. In future research this system could be used to locally tailor melt pool depth in laser welding, width of hardened tracks in laser transformation hardening or microstructure of deposited tracks in Laser-based Directed Energy Deposition.

CRediT authorship contribution statement

Scholte J.L. Bremer: Writing – original draft, Visualization, Validation, Software, Resources, Methodology, Investigation, Formal analysis, Data curation, Conceptualization, Writing – review & editing. **Ronald G.K.M. Aarts:** Writing – review & editing, Supervision. **Gertwillem R.B.E. Römer:** Writing – review & editing, Supervision, Project administration, Methodology, Funding acquisition, Conceptualization.

Declaration of competing interest

The authors declare that they have no known competing financial interests or personal relationships that could have appeared to influence the work reported in this paper.

Data availability

Data will be made available on request.

Acknowledgements

This research was carried out under project number P16-46/S17024m, which is part of Aim2XL program (www.m2i.nl/aim2xl/), in the framework of the Partnership Program of the Materials innovation institute M2i (www.m2i.nl) and the Netherlands Organization for Scientific Research (www.nwo.nl). The research was conducted in collaboration with industrial partners and supported by the Rotterdam Fieldlab Additive Manufacturing BV (RAMLAB), www.ramlab.com.

References

[1] J.C. Ion, Laser processing diagrams, in: J.C. Ion (Ed.), Laser Processing of Engineering Materials, first ed., Butterworth-Heinemann, Oxford, United Kingdom, 2005, pp. 178–187, http://dx.doi.org/10.1016/B978-075066079-2/50009-X, (Chapter 6).

[2] J.C. Ion, Laser transformation hardening, Surf. Eng. 18 (1) (2002) 14–31, http://dx.doi.org/10.1179/026708401225001228.

[3] T. DebRoy, H.L. Wei, J.S. Zuback, T. Mukherjee, J.W. Elmer, J.O. Milewski, A.M. Beese, A. Wilson-Heid, A. De, W. Zhang, Additive manufacturing of metallic components – process, structure and properties, Prog. Mater. Sci. 92 (2018) 112–224, http://dx.doi.org/10.1016/j.pmatsci.2017.10.001.

[4] B. Fotovvati, S.F. Wayne, G. Lewis, E. Asadi, A review on melt-pool characteristics in laser welding of metals, Adv. Mater. Sci. Eng. 2018 (2018) 4920718, http://dx.doi.org/10.1155/2018/4920718.

[5] A.R. Konuk, R.G.K.M. Aarts, A.J. Huis in 't Veld, T. Sibillano, D. Rizzi, A. Ancona, Process control of stainless steel laser welding using an optical spectroscopic sensor, Physics Procedia 12 (2011) 744–751, http://dx.doi.org/10.1016/j.phpro.2011.03.093.

[6] Z. Smoqi, B.D. Bevans, A. Gaikwad, J. Craig, A. Abul-Haj, B. Roeder, B. Macy, J.E. Shield, P. Rao, Closed-loop control of meltpool temperature in directed energy deposition, Mater. Des. 215 (2022) 110508, http://dx.doi.org/10.1016/J.MATDES.2022.110508.

[7] S. Kou, Weld metal solidification I: Grain structure, in: Welding Metallurgy, second ed., John Wiley & Sons, Inc., Hoboken, New Jersey, USA, 2002, pp. 170–198, http://dx.doi.org/10.1002/0471434027.ch7, (Chapter 7).

[8] M.H. Farshidianfar, F. Khodabakhshi, A. Khajepour, A.P. Gerlich, Closed-loop control of microstructure and mechanical properties in additive manufacturing by directed energy deposition, Mater. Sci. Eng. A 803 (2021) 140483, http://dx.doi.org/10.1016/j.msea.2020.140483.

[9] J.I. Arrizubieta, S. Martínez, A. Lamikiz, E. Ukar, K. Arntz, F. Klocke, Instantaneous powder flux regulation system for laser metal deposition, J. Manuf. Process. 29 (2017) 242–251, http://dx.doi.org/10.1016/j.jmapro.2017.07.018.

[10] J. Pu, Y. Zhao, Y. Jiang, J. Zou, S. Song, Influence of wire feeding speed on the melting behavior and formation of narrow-gap joint by laser welding with filler wire, J. Laser Appl. 32 (3) (2020) 032007, http://dx.doi.org/10.2351/7.0000043.

[11] S.J.L. Bremer, M. Luckabauer, G.R.B.E. Römer, Laser intensity profile as a means to steer microstructure of deposited tracks in directed energy deposition, Mater. Des. 227 (2023) 111725, http://dx.doi.org/10.1016/j.matdes.2023.111725.

[12] J. Sundqvist, A.F.H. Kaplan, L. Shachaf, C. Kong, Analytical heat conduction modelling for shaped laser beams, J. Mater Process. Technol. 247 (2017) 48–54, http://dx.doi.org/10.1016/j.jmatprotec.2017.04.011.

[13] S.M. Thompson, L. Bian, N. Shamsaei, A. Yadollahi, An overview of direct laser deposition for additive manufacturing; part I: Transport phenomena, modeling and diagnostics, Addit. Manuf. 8 (2015) 36–62, http://dx.doi.org/10.1016/j.addma.2015.07.001.

[14] P. Haug, S. Weidgang, J. Seebach, N. Speker, T. Hesse, S. Bisch, Beam shaping BrightLine weld – latest application results, in: LiM 2019 Proceedings, 2019.

[15] H. Hagino, S. Shimizu, H. Ando, H. Kikuta, Design of a computer-generated hologram for obtaining a uniform hardened profile by laser transformation hardening with a high-power diode laser, Precis. Eng. 34 (3) (2010) 446–452, http://dx.doi.org/10.1016/j.precisioneng.2009.11.001.

[16] H.S. Dewi, A. Fischer, J. Volpp, T. Niendorf, A.F.H. Kaplan, Microstructure and mechanical properties of laser surface treated 44MnSiVS6 microalloyed steel, Opt. Laser Technol. 127 (2020) 106139, http://dx.doi.org/10.1016/j.optlastec.2020.106139.

[17] C. Goppold, T. Pinder, P. Herwig, Transient beam oscillation with a highly dynamic scanner for laser beam fusion cutting, Adv. Opt. Technol. 5 (1) (2016) 61–70, http://dx.doi.org/10.1515/aot-2015-0059.

[18] P. Horník, H. Šebestová, J. Novotný, L. Mrňa, Laser beam oscillation strategy for weld geometry variation, J. Manuf. Process. 84 (2022) 216–222, http://dx.doi.org/10.1016/J.JMAPRO.2022.10.016.

[19] P. Sancho, F. Cordovilla, J. Dominguez, M.Á. Montealegre, J. Isaza, Á. García-Beltrán, J.L. Ocaña, Customized laser beam intensity distribution for the laser surface treatment of geometrically convoluted components, J. Mater Process. Technol. 263 (2019) 223–232, http://dx.doi.org/10.1016/J.JMATPROTEC.2018.08.020.

[20] C. Prieto, E. Vaamonde, D. Diego-Vallejo, J. Jimenez, B. Urbach, Y. Vidne, E. Shekel, Dynamic laser beam shaping for laser aluminium welding in e-mobility applications, Procedia CIRP 94 (2020) 596–600, http://dx.doi.org/10.1016/j.procir.2020.09.084.

[21] A. Nissenbaum, N. Armon, E. Shekel, Dynamic beam lasers based on coherent beam combining, in: C. Jáuregui-Misas, V.R. Supradeepa (Eds.), in: Fiber Lasers XIX: Technology and Systems, vol. 11981, SPIE, 2022, 119810B, http://dx.doi.org/10.1117/12.2608218.

[22] M. Meunier, A. Kumar, A. Lucas, S. Bernard, R. Arias, J.L. Arias Otero, G. Pallier, G. Labroille, Stainless steel laser beam welding with a dynamic tailored beam shaping laser-head based on multi-plane light conversion, in: LiM 2023 Proceedings, 2023, p. 21, http://dx.doi.org/10.1117/12.2655458.

[23] Y. Mi, P. Guglielmi, M. Nilsen, F. Sikström, G. Palumbo, A. Ancona, Beam shaping with a deformable mirror for gap bridging in autogenous laser butt welding, Opt. Lasers Eng. 169 (2023) 107724, http://dx.doi.org/10.1016/j.optlaseng.2023.107724.

[24] G. Vdovin, M. Loktev, A. Simonov, Low-cost deformable mirrors: technologies and goals, in: M.T. Gruneisen, J.D. Gonglewski, M.K. Giles (Eds.), in: Advanced Wavefront Control: Methods, Devices, and Applications III, vol. 5894, 2005, 58940B, http://dx.doi.org/10.1117/12.621042.

[25] O. Pütsch, J. Stollenwerk, P. Loosen, Integrated optical design for highly dynamic laser beam shaping with membrane deformable mirrors, Laser Reson. Microreson. Beam Control XIX 10090 (February 2017) (2017) 1009010, http://dx.doi.org/10.1117/12.2256127.

[26] A. Bäuerle, A. Bruneton, R. Wester, J. Stollenwerk, P. Loosen, Algorithm for irradiance tailoring using multiple freeform optical surfaces, Opt. Express 20 (13) (2012) 14477, http://dx.doi.org/10.1364/OE.20.014477.

[27] S.J.L. Bremer, R.G.K.M. Aarts, G.R.B.E. Römer, Mathematical analysis of dynamic high power laser beam shaping using galvanometer scanners or deformable mirrors, 2023, http://dx.doi.org/10.2139/ssrn.4595382.

[28] M. Pastore, A. Calcagnì, Measuring distribution similarities between samples : A distribution-free overlapping index, Front. Psychol. 10 (2019) 1089, http://dx.doi.org/10.3389/fpsyg.2019.01089.

[29] G. Vdovin, O. Soloviev, A. Samokhin, M. Loktev, Correction of low order aberrations using continuous deformable mirrors, Opt. Express 16 (5) (2008) 2859–2866, http://dx.doi.org/10.1364/OE.16.002859.